

# Dynamic motion monitoring of a 3.6 km long steel rod in a borehole during cold-water injection with distributed fiber-optic sensing

Martin P. Lipus<sup>1</sup>, Felix Schölderle<sup>2</sup>, Thomas Reinsch<sup>3,1</sup>, Christopher Wollin<sup>1</sup>, Charlotte M. Krawczyk<sup>1,4</sup>, Daniela Pfrang<sup>2</sup>, Kai Zosseder<sup>2</sup>

<sup>1</sup>GFZ German Research Centre for Geosciences, Telegrafenberg, 14473 Potsdam, Germany

<sup>2</sup>Technical University Munich, Hydrogeology and Geothermal Energy, Arcisstr. 21, 80333 Munich, Germany

<sup>3</sup>present address: Fraunhofer IEG, Fraunhofer Research Institution for Energy Infrastructures and Geothermal Systems IEG, Am Hochschulcampus 1 IEG, 44801 Bochum, Germany

<sup>4</sup>Technical University (TU) Berlin, Institute for Applied Geosciences, Ernst-Reuter-Platz 1, 10587 Berlin, Germany

## Abstract

Fiber-optic distributed acoustic sensing (DAS) data finds many applications in wellbore monitoring such as e.g. flow monitoring, formation evaluation, and well integrity studies. For horizontal or highly deviated wells, wellbore fiber-optic installations can be conducted by mounting the sensing cable to a rigid structure (casing/tubing) which allows for a controlled landing of the cable. We analyze a cold-water injection phase in a geothermal well with a 3.6 km long fiber-optic installation mounted to a 3/4" sucker-rod by using both DAS and distributed temperature sensing (DTS) data. During cold-water injection, we observe distinct vibrational events (shock waves) which originate in the reservoir interval and migrate up- and downwards. We use temperature differences from the DTS data to determine the theoretical thermal contraction and integrated DAS data to estimate the actual deformation of the rod construction. The results suggest that the rod experiences thermal stresses along the installation length – partly in the compressional and partly in the extensional regime. We find strong evidence that the observed vibrational events originate from the release of the thermal stresses when the friction of the rod against the borehole wall is overcome. Within this study, we show the influence of temperature changes on the acquisition of distributed acoustic/strain sensing data along a fiber-optic cable suspended along a rigid but freely hanging rod. We show that observed vibrational events do not necessarily originate from induced seismicity in the reservoir, but instead, can originate from stick-slip behavior of the rod construction that holds the measurement equipment.

## 1. Introduction

Fiber-optic distributed sensing in bore-hole applications has gained a lot of attention in the recent years. Distributed temperature sensing (DTS) has been used to assess rock thermal properties and locations of water-bearing fractures (e.g. [Hurtig, 1994](#), [Förster, 1997](#)). DTS was used to perform cement job evaluations and wellbore integrity analysis during and after production tests (e.g. [Pearce et al., 2009](#), [Bücker and Großwig, 2017](#)). The performance of a borehole heat exchanger was monitored with DTS to evaluate the heat input along the wellbore and to measure the regeneration time after a heat extraction period ([Storch et al., 2010](#)). While DTS has found its way as a standard tool for wellbore monitoring over the last two decades, the utilization of distributed acoustic sensing (DAS) is still subject to many research questions. [Johannessen et al., 2012](#) introduced the potential and capabilities for acoustic in-well monitoring applications based on DAS systems which range from e.g. flow measurements, sand detection, gas breakthrough, leak detection to vertical seismic profiling (VSP). [Daley et al., 2013](#), [Mateeva et al., 2014](#), [Harris et al., 2016](#), [Daley et al., 2016](#) and [Henninges et al., 2021](#) compare traditional geophone with DAS recordings acquired during a vertical seismic profiling campaign (VSP). [Götz et al., 2018](#) report on a multi-well VSP campaign at a carbon dioxide storage site by using only one single DAS interrogator. [Finfer et al., 2014](#) performed an experiment to study DAS applications for turbulent single-phase water flow monitoring in a steel pipe. [Bruno et al., 2018](#) investigate the potential to use downhole DAS data for cross-hole monitoring between two adjacent wells by inducing low frequency pressure pulses to detect high conductivity zones by measuring characteristic vertical strain patterns. [Naldrett et al., 2018](#) compare fiber-optic technology to traditional production logging tools and provides field data examples of flow monitoring based on both DTS and DAS with wireline-type installations. [Ghahfarokhi et al., 2019](#) analyze an extensive data set including borehole geophone and DAS during hydraulic fracturing (cable behind casing) to study micro-seismicity and low frequency events in the borehole. [Raab et al., 2019](#) shows that DAS data from a behind casing installation can be correlated to conventional cement-bond-log (CBL) recordings by analyzing the acoustic data in noisy drilling and testing operations. [Chang](#)

55 [et al., 2020](#) and [Martuganova et al., 2021](#) report on reverberating signals in DAS recordings which can occur on  
56 free-hanging cables in geothermal wells during fluid injection and which are probably caused by bad cable-to-well  
57 coupling. In all reported cases, the coupling of the sensing glass fiber to the surrounding media plays a crucial role  
58 for the application of DAS technology.

59 Especially for the monitoring of deformations occurring over longer time periods, i.e. from minutes to hours to  
60 days, the coupling of cable and surrounding environment becomes essential to derive any meaningful result from  
61 fiber-optic strain sensing. Where as [Reinsch et al., 2017](#) provide a theoretical approach to describe the response of  
62 the sensing fiber in dependence of the specific cable design, the coupling of the cable to the rock formation strongly  
63 depends on the specifics of a measuring experiment. [Lipus et al., 2018](#) compare data from fiber-optic strain sensing  
64 and data from conventional gamma-gamma-density wire-line log during a gravel packing operation in a shallow  
65 well for heat storage. [Sun et al., 2020](#) demonstrate with a laboratory and field test that the extent of a deformed  
66 reservoir sandstone and silt caprock by injected CO<sub>2</sub> can be quantitatively evaluated using static distributed strain  
67 sensing over periods of 42 hours (cable behind casing). [Zhang et al., 2020](#) provide an attempt to use distributed  
68 strain sensing to monitor elastic rock deformation during borehole aquifer testing to derive hydraulic parameter  
69 information. [Miller et al., 2018](#) compare DTS and time-integrated DAS recordings from a borehole and finds a  
70 correlation between DTS recordings and very low frequent DAS strain recordings. In their work, they report on  
71 repeating “slip events” seen in the DAS data as short and confined vibrational events upon temperature changes  
72 in the well.

73 The study at hand observes similar “slip events” and shows their causal connection to the thermo-mechanical  
74 response of the borehole construction to water flow therein.

75  
76 Installing a fiber-optic cable in a borehole requires specialized equipment. Depending on the aim of the fiber-optic  
77 monitoring campaign, different cable installation types are possible. One way is to permanently install the cable  
78 by mounting it to the outside of a casing and run it together with the casing into the well and cement it in place  
79 (e.g. [Henninges et al. 2005](#), [Reinsch et al., 2013](#), [Lipus et al., 2021](#)). A cemented fiber-optic cable generally  
80 provides a thorough mechanical coupling to the surrounding structure which is favorable for DAS data quality.  
81 Due to its placement behind the casing, the fibers do not interfere with well operations and monitoring of the well  
82 can be performed at any time. However, the cemented annulus of a well is a crucial secondary barrier element for  
83 well integrity which is compromised by the installation of a fiber-optic cable. A fluid pathway could potentially  
84 be created along the cable. cases where the well completion design includes liner elements, a permanent cable  
85 installation behind casing to the end of the well is technically not possible, or at least, very challenging. In such  
86 cases, other installation types are available. A semi-permanent installation along e.g. a production tubing or a  
87 temporary installation via a wireline cable or coiled tubing allow cable placements inside the borehole after drilling  
88 is finished. [Munn et al., 2017](#) present a field test of a novel “flexible borehole coupling technique” that allows  
89 deploying fiber-optic cables in boreholes after completion has finished with an improved mechanical coupling  
90 compared to lose installed fiber-optic cables. Due to physical constrains, this technology is best suited for shallow  
91 boreholes (< 425 m). [Becker et al. 2017](#) provide an analysis of borehole fracture displacements using such kind of  
92 cable coupling technique. Another method to land a fiber-optic cable into a well is by mounting it to a rigid rod  
93 (e.g. a pump sucker-rod). The stiff sucker-rod acts as a centralizer and guides the flexible fiber preventing it from  
94 coiling up. Such type of installation is especially advantageous when the cable should be placed in a deep and  
95 deviated well.

96  
97 To utilize acquired fiber-optic data from a free-hanging/free-lying rod with the highest possible confidence, it is  
98 important to understand the behavior of such a long and stiff structure inside a well. Heating and/or cooling of the  
99 well will lead to thermal stresses in the material which potentially result in contraction or expansion of the sucker-  
100 rod and fiber-optic cable construction. As the fiber-optic cable is firmly attached to the rods, these dynamics  
101 influence the distributed strain and temperature sensing. From DTS monitoring, [Schölderle et al., 2021](#) found that  
102 measurement equipment in the previously described setting does indeed contract upon the injection of cold water  
103 and that the points spatially sampled by the distributed sensing change their position. Besides a detailed analysis  
104 based on DAS and DTS data of the rod’s dynamics in response to temperature changes during a cold-water  
105 injection, we show that the resulting thermal stresses are released by the observed vibrational events thus indicating  
106 stick-slip like behavior of the rod-borehole wall compound.

## 107 108 **1.1 Well description and cable installation**

109  
110  
111  
112  
113  
114  
115  
116  
117  
118  
119  
120

The fiber-optic cable is installed within a production well at the geothermal site Schäftlarnstraße in Munich, Germany. A detailed description of the geothermal site and the cable installation procedure is presented in [Schölderle et al., 2021](#). The well was completed with a 20" anchor casing, a 13 3/8", a 9 5/8" liner and a perforated 7" production liner. An overview of the landing depths is presented in Table 1. The design of the borehole completion is schematically shown in Figure 3 (right subplot). The well is vertical to a depth of 250 m. Below 250 m, the well is slightly inclined to 4° down to a depth of 879 m TVD (880 m MD). A number of kick-off-points (KOP) are located along the well path. These are also listed in Table 2. In the result section, a survey shows the well path. From a flow-meter log it is known, that the most prominent feed zone in the well is just below the transition from 9 5/8" liner to 7" perforated liner in the depth interval between 2825 - 2835 m MD.

Table 1: Well design at geothermal site Schäftlarnstraße, Munich (see also Figure 3)

Drill bit Ø	Type	Casing/liner Ø	Top (TVD / MD) [m]	Bottom (TVD / MD) [m]
	Stand-pipe	30"	surface	59.1 / 59.1
26"	Anchor casing	20"	surface	866.2 / 867.5
17 1/2"	Liner	13 3/8"	766.0 / 767.0	1812.3 / 2010.0
12 1/4"	Liner	9 5/8"	1740.0 / 1907.2	2408.7 / 2819.0
8 1/2"	Perforated liner	7"	2412.2 / 2810.1	2932.7 / 3716.0

KOP	Inclination [°]	Depth (TVD / MD) [m]	Direction [°]
#1	44	879 / 880	287
#2	42	1819 / 2220	250
#3	58	2432 / 2850	250
#4	57	2775 / 3432	231

121  
122  
123  
124  
125  
126  
127  
128  
129  
130  
131  
132  
133  
134  
135  
136  
137  
138  
139  
140  
141  
142  
143  
144

The downhole fiber-optic cable is a tubing-encapsulated-fiber (TEF) that contains two multi-mode and two single-mode fibers. In this fiber-in-metal-tube (FIMT) construction, the sensing fibers are embedded in gel and placed in a metal tube. At elevated strain levels, the gel deforms plastically and allows for a relative motion between fiber and cable. Also, creep between cable construction and optical fibers can occur. Strain measurements with such a type of cable are typically applicable for dynamic strain changes (high frequencies) and low deformations ([Reinsch et al. 2017](#)). For longer periods and higher deformations, fiber-optic strain sensing with FIMT cables is still possible but it becomes less localized due to deformation of the material. A laboratory experiment on the relative motion between cable structure and optical fiber in a FIMT cable at higher mechanical stress over time is presented in literature ([Lipus et al., 2018](#)). The cable has a total nominal diameter of 0.43 inch (1.1 cm) and the cable mantle is made of polypropylene. The cable was landed in the well after drilling was finished. To safely and effectively navigate the placement of the fiber-optic cable down to the end of the almost 3.6 km long well, the cable was strapped to steel rods (sucker rods) which were installed in the well together with the cable. The steel sucker rod also helps to retrieve the cable from the bore-hole when needed. Due to the high deviations in the well at depth, the cable needs to be gently pushed into the well. Therefore, the rigid sucker rod is used for the installation instead of a wireline-type installation. The final landing depth of the sucker rod construction is 3691 m (MD). Figure 1 depicts the configuration of the sucker rod/fiber-optic compound. Together with a number of cross-over elements and the final landing joint, more than 400 of individual sucker rod elements were installed in the well. In the following, we refer to the sucker rod / fiber-optic cable construction as "the rod". The depth reference for the DTS (spot warming) and DAS (tap test) are set to surface.

A fiber-optic pressure/temperature (p/T) gauge was installed with the rod and positioned at the top of the reservoir section at 2755 m (MD).

## 1.2 Monitoring campaign

145  
146  
147  
148  
149

The data shown in this study was measured before and during a cold-water injection test in a geothermal well. Before the start of fluid injection, the well was shut-in for 29 days, so that the initial temperature profile is close to the natural geothermal gradient of the Bavarian Molasse basin (see [Schölderle et al., 2021](#)). The temperature at

150 the well head was 17 °C and increasing up to 110 °C at the bottom of the well just before the injection start (see  
151 profile “00:48” in left panel in Figure 4). Cold-water fluid injection started on January 23, 2020 at 00:56 by  
152 pumping water through the wellhead which leads to a cooling of the well. With an initial water table at a depth of  
153 170m below surface, water was injected from the surface without pressure built-up at the wellhead. The cold-water  
154 injection was maintained for 24h at a flow rate of 83 m<sup>3</sup>/h. In this study, we analyze the transient phase of well  
155 temperature change for the first 72 minutes of cold-water fluid injection.  
156



157  
158 *Figure 1: Down-hole cable configuration of the sucker rod with a centralizer (black) and the fiber-optic cable*  
159 *(yellow)*

157  
158  
159

160

## 161 2. Data Analysis

162

163 The analysis in this study is based on the comparison of strain derived from fiber-optic distributed temperature  
164 sensing (DTS) on the one hand and distributed acoustic sensing (DAS) on the other.

165

### 166 2.1 Derivation of strain from DTS

167

168 DTS uses each location of a glass fiber as a sensor for temperature ([Hartog, 1983](#), [Hartog and Gamble, 1991](#)).  
169 This is achieved by coupling laser-light pulses into a glass fiber and analyzing the Raman spectrum of the  
170 backscattered light whose origin along the fiber is determined by the two-way travel time of the light. In this study,  
171 we use a system based on Raman backscatter. Temperature profiles were acquired every 10 minutes with a spatial  
172 sampling of 0.25 m. Detailed information about the performance of the fiber-optic system and the calibration  
173 procedure are presented in [Schölderle et al., 2021](#).

174 We calculate the change in temperature from DTS at the start of fluid injection and the profile later during fluid  
175 injection. From DTS measurements we may predict thermo-mechanical deformation according to

$$176 \varepsilon_{DTS}(x) = \alpha_{rod} \cdot \Delta T(x) \quad (1)$$

177 where  $\alpha_{rod}$  is the thermal expansion coefficient and  $\Delta T(x)$  is the temperature difference at two subsequent points  
178 in time at some location  $x$  of the fiber. The rod construction as a whole consists of many different materials with  
179 different thermal expansion coefficients, such as the sensing fibers, gel filling, metal tubes, polypropylene mantle,  
180 steel rod and nylon centralizers. However, the steel of the sucker rod and the steel of the fiber-optic mantle are the  
181 dominant material by weight and the most relevant for any thermal stresses. The sucker rod consists of 4332 SRX  
182 Nickel Chromium Molybdenum steel with a thermal expansion coefficient of 10 - 13  $\mu\text{e}/\text{K}$  ([Hidnert, 1931](#)) and a  
183 modulus of elasticity of 200 GPa ([T.E. Toolbox, 2012](#)). The second most dominant material is the polypropylene  
184 cable mantle with a modulus of elasticity of 1.5-2 GPa ([T.E. Toolbox, 2012](#)). The proportion of steel on the thermal  
185 stresses in the rod construction are 99.8%. For simplicity, we assume that thermal expansion coefficient  $\alpha_{rod} = 13$   
186  $\mu\text{e}/\text{K}$  for the sucker rod / fiber-optic cable construction and neglect the other materials.

### 187 2.2 Direct measurement of strain via DAS

188 Similar to DTS, DAS also analyzes the back scatter of light coupled into a fiber from one end. Upon contraction  
189 or dilatation, the strain-rate of the fiber, i.e. the temporal derivative of relative change of length, can be derived  
190 from the temporal change of the interference pattern of coherent light elastically scattered (Rayleigh scattering)  
191 from adjacent points within a certain interval of fiber called the gauge length ([Masoudi et al., 2013](#)). The centroid  
192 of the gauge length is defined as a sensor node. The location ( $x$ ) of a sensor node along the fiber is again determined  
193 by the two-way travel time of light from its source to the node and back. In our study, DAS data is acquired at

194 10000 Hz and down-sampled to 1000 Hz. The gauge length and spatial sampling are 10 m and 1 m, respectively.  
 195 No additional filtering was applied in post-processing (no high pass and no low pass filtering).  
 196 In contrast to DTS, DAS directly yields the temporal derivative of strain. In order to convert the measured strain  
 197 rate  $\dot{\epsilon}(x,t)$  data to strain  $\epsilon_{DAS}(x)$  at each location, we integrate in time:

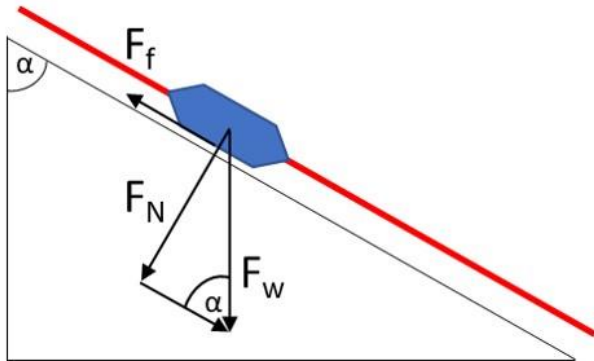
$$198 \epsilon_{DAS}(x) = \int_{t_1}^{t_2} \dot{\epsilon}(x, t) dt \quad (2)$$

199 where  $t_1$  and  $t_2$  delineate the time window and  $\dot{\epsilon}(x,t)$  the recorded strain rate at position  $x$ . In the following we  
 200 speak of “measured strain”  $\epsilon_{DAS}$  in contrast to “predicted or expected” strain  $\epsilon_{DTS}$ .

201 We compare  $\epsilon_{DTS}$  with  $\epsilon_{DAS}$  measurements. We then use the  $\epsilon_{DTS}$  data to compute the contractional forces along the  
 202 rod which occur due to cooling. We compare the result with a static friction curve that was estimated from the  
 203 sucker rod tally and borehole inclination.

### 204 205 2.3 Stick-slip approach

206  
 207 As the thermal contraction of the cooled sucker rod inflicts a sliding movement of the rods along the borehole  
 208 wall, we must consider the friction of their relative motion. This friction would yield a stick-slip motion which is  
 209 observed almost everywhere when two solid objects are moving relative to one another. A detailed review of the  
 210 origins of stick-slip behavior in mechanical parts as well as an experimental and theoretical analysis on stick-slip  
 211 characteristics is presented in literature (e.g. [Berman et al., 1995](#)). In the simplest case, a stick-slip motion appears  
 212 when the static friction force  $F_f$  between two stationary solid bodies is overcome. A schematic drawing of the  
 213 forces on an interval of the sucker-rod construction at a depth with borehole inclination is presented in Figure 2.  
 214



215  
 216 *Figure 2: Static friction force  $F_f$  and normal force  $F_N$  applying on a sucker-rod contact point (nylon centralizer) as a*  
 217 *function of the weight force  $F_w$  and the borehole inclination  $90^\circ - \alpha$*

218  
 219 The static friction force  $F_f$  can be calculated according to

$$220  
221 F_f = \mu \cdot F_N \quad (3)$$

222 where  $F_n$  is the normal force and  $\mu$  the static friction coefficient. The value for  $\mu = 0.36$  was obtained from a plate-  
 223 to-plate experimental analysis on the stick-slip behavior between steel and glass fiber-reinforced nylon specimen  
 224 ([Muraki et al., 2003](#)). The force  $F_N$  is calculated according to

$$225  
226 F_N = F_w \cdot \sin\alpha = g \cdot m \cdot \sin\alpha \quad (4)$$

227  
 228 where  $F_w$  is the gravitational weight force and  $\alpha$  the borehole inclination. Each sucker rod element is 9.1 m long,  
 229 weights 15.7 kg and is equipped with four nylon centralizers and the fiber-optic cable (20 g/m). Therefore, the  
 230 weight force for each contact point of the rod construction yields  $F_w = 9.81 \text{ m/s}^2 \cdot 15.9 \text{ kg} / 4 = 39.0 \text{ N}$ . Regarding  
 231 the lowermost part of the rod construction as an example, this means that for the last nylon centralizer (borehole  
 232 inclination of  $54^\circ$ ), a static friction force of  $F_f = 0.36 \cdot 39.0 \text{ N} \cdot \sin(54^\circ) = 11.3 \text{ N}$  is calculated. With respect to  
 233 contraction of an initially unstressed rod construction, for each subsequent nylon centralizer towards the surface,  
 234 the friction force of the rod at the given depth is calculated by the cumulative sum of all friction forces from the  
 235 nylon centralizers below. The friction force increases with decreasing well depth. Two further weights are added  
 236 to the friction force profile: the bottom end of the sucker rod is a 1.4 m long steel piece with a weight of 64 kg and

237 the carrier of the pT gauge at 2755 m MD is a 2.2 m long steel piece with a weight of 105 kg. Here, we applied a  
 238 static friction coefficient for steel on steel of  $\mu = 0.8$  ([Lee and Polycarpou, 2007](#)).  
 239

240 The expected thermal contraction  $\varepsilon_{DTS}$  can also be translated to a force. Assuming a Young’s modulus for stainless  
 241 steel of  $E = 200$  GPa ([Cardarelli, 2018](#)) and given the cross-sectional area of the rod ( $A_{rod} = 2.9$  cm<sup>2</sup>), we can  
 242 calculate the applied force  $F_{app}$  at each location along the rod which was thermally induced within the investigated  
 243 one-hour cold-water injection period:  
 244

$$245 F_{app} = \sigma \cdot A_{rod} = E \cdot \varepsilon_{DTS} \cdot A_{rod} \quad (5)$$

246  
 247 For simplicity, we assume that the elasticity from the fiber-optic cable and the nylon centralizers are neglectable  
 248 and that the steel dominates the mechanical behavior of the structure. Furthermore, we make the assumption that  
 249 no mechanical stresses are exerted on the rod prior to the cold-water injection. This allows us to set a zero-force  
 250 baseline before injection start for the stick-slip analysis.  
 251

## 252 2.4 Stick-slip event detection and picking

253  
 254 In the DAS data we monitored repeating vibrational events with ongoing cold-water injection in the deeper part of  
 255 the well. These events are characterized by a sudden DAS amplitude peak at some depth and an up- and downward  
 256 directed move-out. With time, the spatio-temporal distribution of these vibrational events changes. To automate  
 257 the detection of depth location and moveout of an event, we employ a short-term/long-term average trigger ([Allen,  
 258 1978, Vaezi and v.d. Baan \(2015\)](#)). The parameters used for the STA/LTA analysis can be found in Table 2:  
 259  
 260

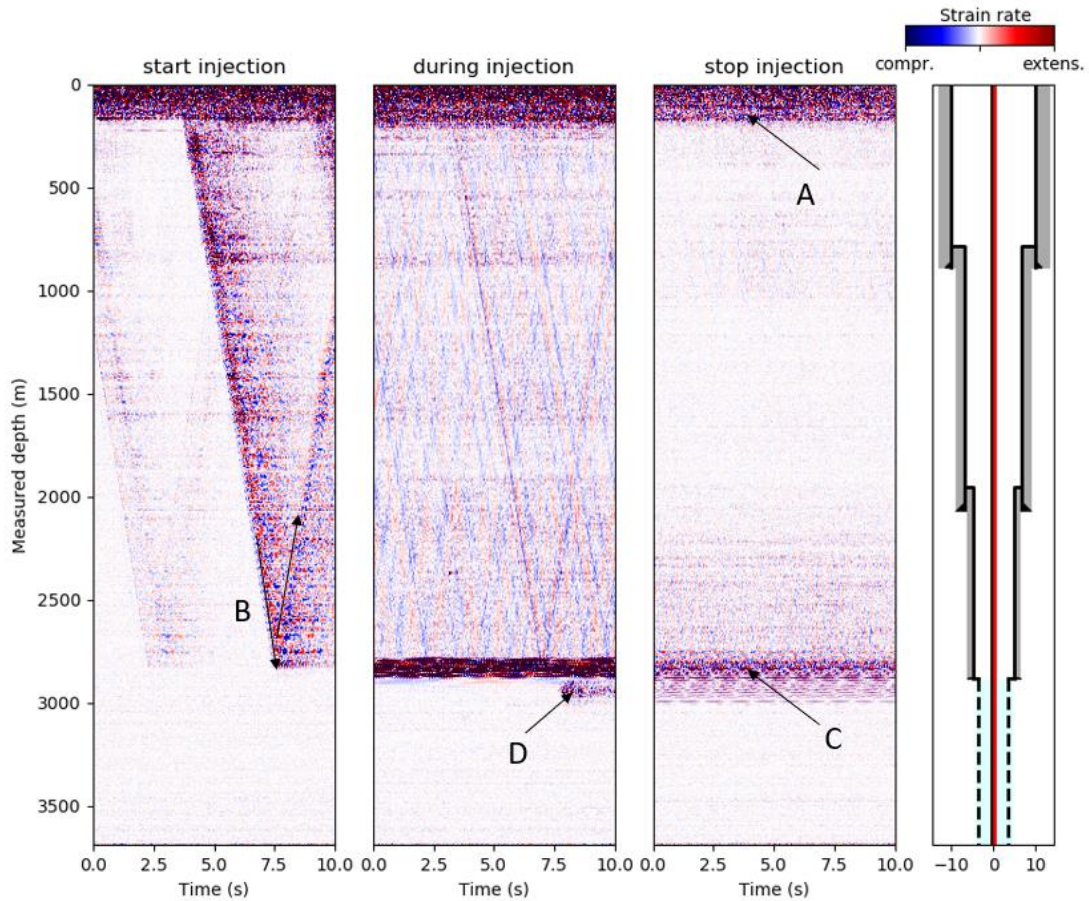
Table 2: Parameters used for the STA/LTA detection method

Parameter	Value
STA window length ( $N_s$ )	1 s (1000 samples)
LTA window length ( $N_L$ )	3 s (3000 samples)
Trigger start threshold $\tau_1$	2
Trigger end threshold $\tau_2$	0.8

261  
 262  
 263  
 264

## 3. Results

265 Figure 3 shows examples of raw and unprocessed strain rate data measured with the DAS unit in the well at the  
 266 start of cold-water injection (1<sup>st</sup> subplot), one hour after start of fluid injection (2<sup>nd</sup> subplot) and shortly after the  
 267 end of the 24 hours water injection period (3<sup>rd</sup> subplot). Each subplot depicts 10 seconds of data with the same  
 268 data color scaling. A number of features can be recognized in each of the data examples. At the depth marked with  
 269 the arrow “A”, there is a transition from a noisy depth interval above to a rather quiet one below. The transition  
 270 marks the location of the water table in the well. From the wellhead, the water free-falls down to the water table  
 271 at about 170 m below surface. In the cased hole section down to the depth of the transition to the perforated liner,  
 272 high velocity tube waves (around 1500 m/s) are present which are reflected at the liner shoe of the 9 5/8” casing  
 273 at ca. 2810 m MD (arrow “B” in first subplot). Below “B”, the cable is located inside the perforated liner. The tube  
 274 waves are not further guided in this interval and the noise level is rather low. In the uppermost 100 m of the  
 275 perforated liner section (2810 – 2900 m MD), a strong signal is present in the 2<sup>nd</sup> and 3<sup>rd</sup> subplot (arrow “C”). The  
 276 arrow “D” marks another common characteristic feature in the DAS data which was observed over the analyzed  
 277 cold-water injection period. This abrupt and localized signal is interpreted as a sudden contraction of the sucker  
 278 rod.



279  
280  
281  
282

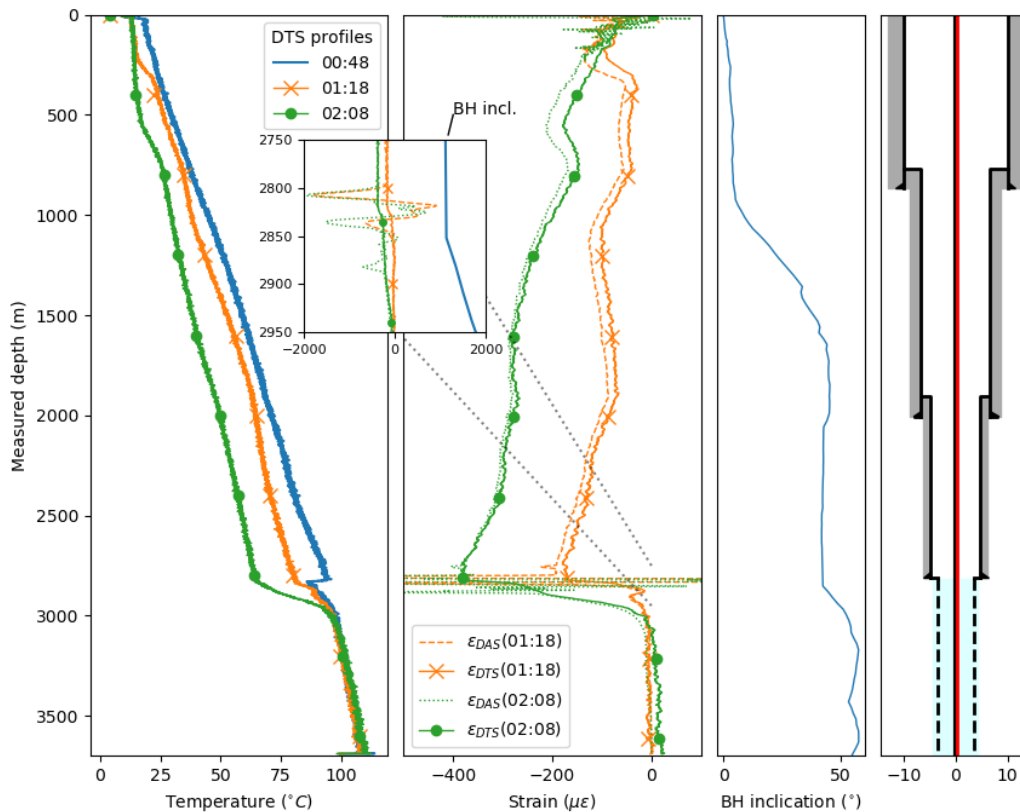
Figure 3: DAS raw data examples over the scope of the cold-water injection phase for (1) the onset of fluid injection (2) ongoing injection and (3) termination of fluid injection. Blue colours show relative compression and red colours relative expansion. The color ranges are the same for all subplots

283  
284

### 3.1 Sucker rod contraction

285  
286  
287  
288  
289  
290  
291  
292  
293  
294  
295

Figure 4 shows fiber-optic data from DTS and DAS for the first hour of cold-water fluid injection testing. The first subplot shows three DTS profiles at 00:48, 01:18 and 02:08, which are -8, +22 and +72 minutes relative to the cold-water injection start. The entire rod from surface to 3100 m experiences cooling. Below the most prominent feed zone of the well at 2830 m MD, the cooling of the well decreases. This is because most of the injected cold-water flows into the formation (2825 - 2835 m MD) and the fluid column below remained rather undisturbed. A theoretical tensile strain from thermal contraction of the steel rod (and the fiber-optic cable)  $\epsilon_{DTS}$  can be derived from the temperature difference between the two profiles for a certain depth relative to the profile at 00:48. The second subplot compares the 15 m moving average of  $\epsilon_{DTS}$  calculated after formula (1) with the local strain ( $\epsilon_{DAS}$ ) calculated after formula (2) during the same time interval. The third subplot shows the borehole inclination from the deviation survey. On the fourth subplot, a schematic representation of the casing/liner landing depths is shown together with the location of the rod.



296

297 *Figure 4: Downhole monitoring data during the cold-water injection test. 1<sup>st</sup> subplot: DTS temperature profiles. 2<sup>nd</sup>*  
 298 *subplot: Comparison of strain profiles  $\epsilon_{DTS}$  and  $\epsilon_{DAS}$ . 3<sup>rd</sup> subplot: borehole inclination. 4<sup>th</sup> subplot: wellbore*  
 299 *schematic*

300 In general, a clear match is visible between  $\epsilon_{DTS}$  and  $\epsilon_{DAS}$  for the entire well which means that the strain the steel  
 301 rod experiences ( $\epsilon_{DAS}$ ) follows the predicted thermal contraction ( $\epsilon_{DTS}$ ). However, there are depth intervals where  
 302 the experienced strain ( $\epsilon_{DAS}$ ) exceeds and others where it falls short on the predicted strain ( $\epsilon_{DTS}$ ). Until 2825-2835  
 303 m MD where the most prominent injection interval is located,  $\Delta T$  increases with increasing depth. At the injection  
 304 interval  $\Delta T$  rapidly increases. Below this zone, no thermal contraction is expected.

305 Along the 13 3/8" casing interval (from top liner hanger 13 3/8" at 768 m MD to top liner hanger 9 5/8" 2010 m  
 306 MD),  $\epsilon_{DTS}$  and  $\epsilon_{DAS}$  are negative and show the same trend thus indicating the expected contraction. In absolute  
 307 values expected strain  $\epsilon_{DTS}$  exceeds the measured strain  $\epsilon_{DAS}$ . Over this depth interval, the well inclination increases  
 308 from nearly vertical to 45°.

309 At the transition to the 7" perforated liner at 2810 m MD (top liner hanger packer) a notably different  $\epsilon_{DAS}$  pattern  
 310 is measured compared to  $\epsilon_{DTS}$  (box plot in Figure 4). In the depth interval 2795-2815 m MD, the expected  
 311 contraction from  $\epsilon_{DTS}$  at 01:18 yields -170  $\mu\epsilon$  (-380  $\mu\epsilon$  at 02:08), while the estimated contraction from  $\epsilon_{DAS}$  at 01:18  
 312 results in -1740  $\mu\epsilon$  (-1950  $\mu\epsilon$  at 02:08)  $\mu\epsilon$  between 2805-2810 m MD, which is more than a factor 10 higher (factor  
 313 5 at 02:08). In the depth interval 2815-2830 m MD,  $\epsilon_{DAS}$  shows an extension of the rod with a maximum of 900  $\mu\epsilon$   
 314 at 01:18 while  $\epsilon_{DTS}$  decreases from -160  $\mu\epsilon$  at 2815 m MD to -55  $\mu\epsilon$  at 2835 m MD. This is the only locations in  
 315 which the integrated strain rate from  $\epsilon_{DAS}$  shows extension instead of the predicted contraction. At 2830-2850 m  
 316 MD, another interval with extraordinary high  $\epsilon_{DAS}$  readings relative to  $\epsilon_{DTS}$  is present. Below 2850 m MD,  $\epsilon_{DAS}$  and  
 317  $\epsilon_{DTS}$  again follow the same trend at 01:18. At 02:08, the  $\epsilon_{DAS}$  and  $\epsilon_{DTS}$  show a discrepancy down to 2890 m MD and  
 318 the same trend below. The gyro data shows a sudden increase in the inclination of the borehole at 2850 m MD.  
 319 Between 2900-3100 m MD, the temperature difference between the two DTS profiles rapidly decreases (see Figure  
 320 4, 1<sup>st</sup> and 2<sup>nd</sup> subplot). At 02:08, the DTS profile shows slightly increased temperatures (+1 °C) with a constant  
 321 offset from 3100 m to the end of the cable compared to the DTS profile at 01:18. This leads to a constant offset of  
 322 a positive expected strain  $\epsilon_{DTS}$ . The measured strain  $\epsilon_{DAS}$  shows no offset in this depth interval.  
 323



## 324 3.2 Sudden contraction events

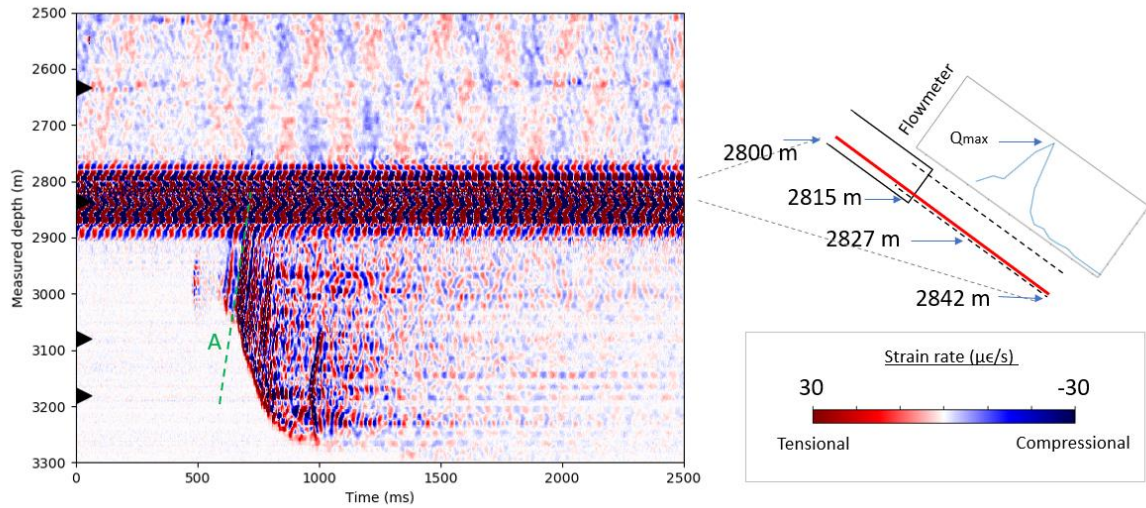
### 325 Event description

326 A close-up of raw DAS data is shown for the depth interval 2500-3300 m MD around the transition from cased  
327 hole to perforated liner 52 minutes after the start of the cold-water fluid injection (see Figure 5). At this time, the  
328 DAS records a transient strain-rate anomaly. Similar events are repeatedly observed in the course of the  
329 measurement during the cold-water injection periods. Using the event shown in Figure 5 as a representative  
330 example, we describe common features of these events in the following. Its origin lies at 600 ms and 3000 m MD  
331 and is characterized by an abrupt increase of the measured strain rate. The sudden increase of strain rate amplitude  
332 propagates both up- and downwards along the well with compressional and tensional sign of amplitude,  
333 respectively, where the propagation velocity upwards is approximately 3900 m/s (green Line A in Figure 5). In  
334 contrast, the downward propagation velocity is slower and shows irregularities from 650-1260 m/s. Most striking  
335 is the decay of the velocity from 3200 m MD onwards and the eventual stop of propagation slightly above 3300 m  
336 MD. In upward direction, this event is halted somewhere in the noisy interval where the reservoir section of the  
337 borehole begins. The event is followed by elastic reverberations that decay after approximately half a second.

338 Further examples of such kind of events are plotted in Figure 6 A, B, C and D. They all have in common, that they  
339 originate below 2900 m MD and trigger a contraction above and an extension below. The previously discussed  
340 event is characterized by a smaller precursor 100 ms before the origin of the large event at the same depth.  
341 Precursors and successors can also be observed in the examples in Figure 6 (in particular in Figure 6 B), yet the  
342 events shown here are distinguished by the fact that their upwards propagation extends beyond the noisy reservoir  
343 section. All exemplary events except 6A whose downward propagation arrests rather sudden, have in common that  
344 the up- and downwards propagation slow down before coming to a halt. Another striking observation in all of the  
345 events is that the initial onset propagates slower than the reverberations in the coda.

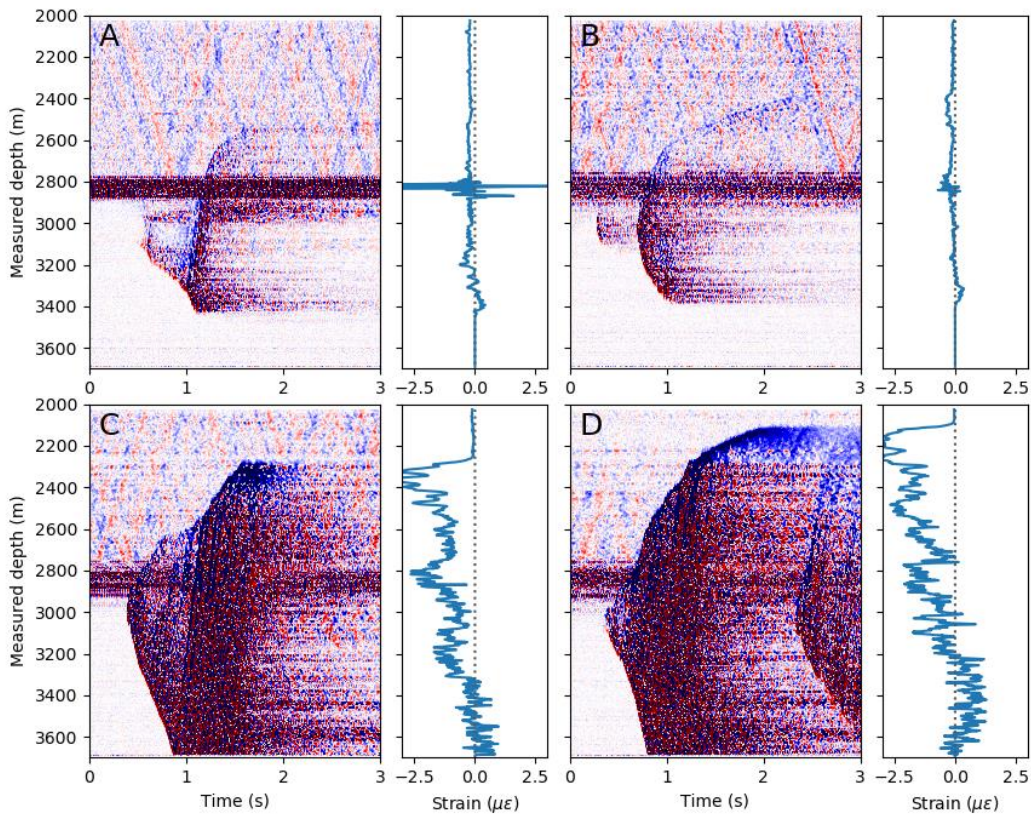
346 While the exact shape of the spatial propagation and length varies (length between 20–1600 m), the duration of  
347 these events is mostly in the range of 0.5 s with some fading noise/reverberation afterwards. These events typically  
348 show a tensional signal at the energy front in the downward direction while the initial energy front upwards is  
349 mostly compressional. As the vibrational signal propagates along the rod, a succession of compressional and  
350 tensional waves is created which moves with a velocity of about 3900 m/s along the rod (as shown by the green  
351 line A in Figure 5). The downward propagation of the first arrival changes its velocity from the onset of the event  
352 towards the end of the vibrational event. In the first 50 ms, it increases in velocity, then it stays constant before it  
353 gradually decreases in velocity at around 700 ms below 3200 m MD.

354 The four black arrows on the left y-axis in Figure 5 indicate the timeseries for which the four spectrograms shown  
355 in Figure 7 were calculated with a moving window of 250 ms. The DAS strain-rate timeseries at 3000 and 3200  
356 m MD show the onset of the slip event at 0.5 s with dominant frequencies of the first break between 30 and 75 Hz.  
357 The slip only lasts approximately half a second but reverberations of different duration and different frequencies  
358 can be observed in band below 30 Hz depending on the rod segment. For instance, at 3000 m MD long lasting  
359 reverberations occur at ~10Hz whereas at 3200 m MD they occur at 20 Hz. As can be seen from the spectrogram  
360 from the DAS strain-rate recordings at 2700 and 2835 m MD, the slip event does not penetrate into and beyond  
361 the feed zone whose characteristic noise at 24 Hz remains undisturbed just as the low frequency pattern of the tube  
362 waves above.



363

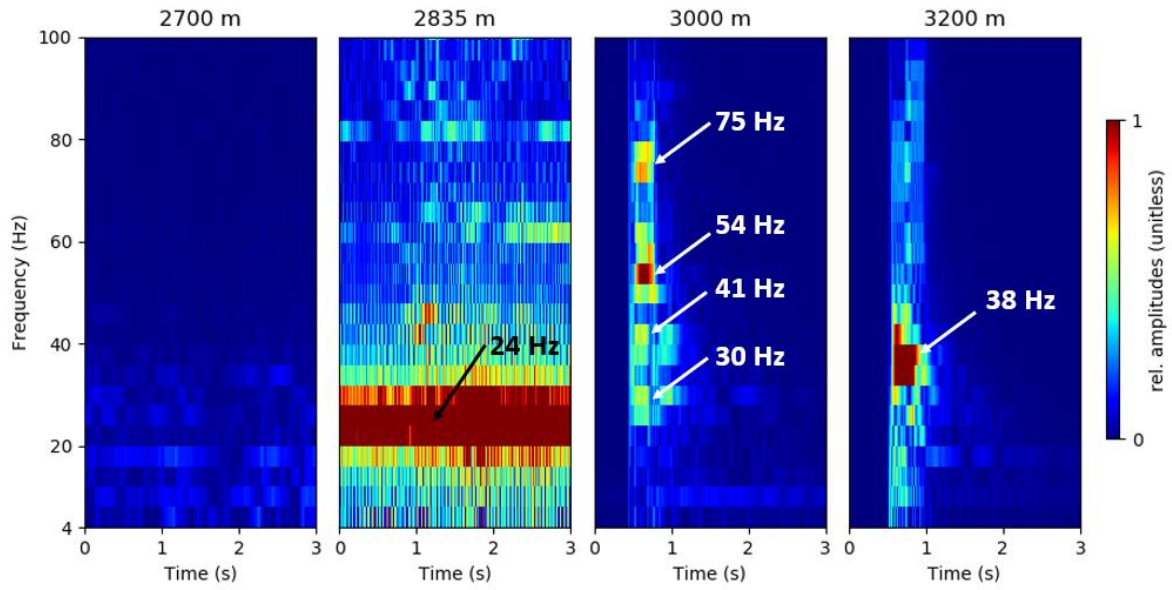
364 *Figure 5: Sucker rod contraction event displayed by strain rate DAS data (left). The black arrows on the left y-axis*  
 365 *mark the depth location of timeseries used for the spectrograms in Figure 7. Line "A" marks the moveout of the*  
 366 *signal at a speed of 4000 m/s. The schematic drawing shows the inclination of the borehole with the fiber-optic*  
 367 *cable (red) lying inside of the casing (right). The inflow profile from a wireline flowmeter measurement is shown by*  
 368 *the blue graph*



369

370 *Figure 6: Four raw DAS data examples of sucker rod events with the integrated strain rate ( $\epsilon_{DAS}$ ) over a period of*  
 371 *3 seconds. The timing of the events relative to the start of cold-water injection is: + 65 minutes B: + 110 minutes*  
 372 *C: + 147 minutes and D: 210 minutes*

373



374  
 375  
 376  
 377

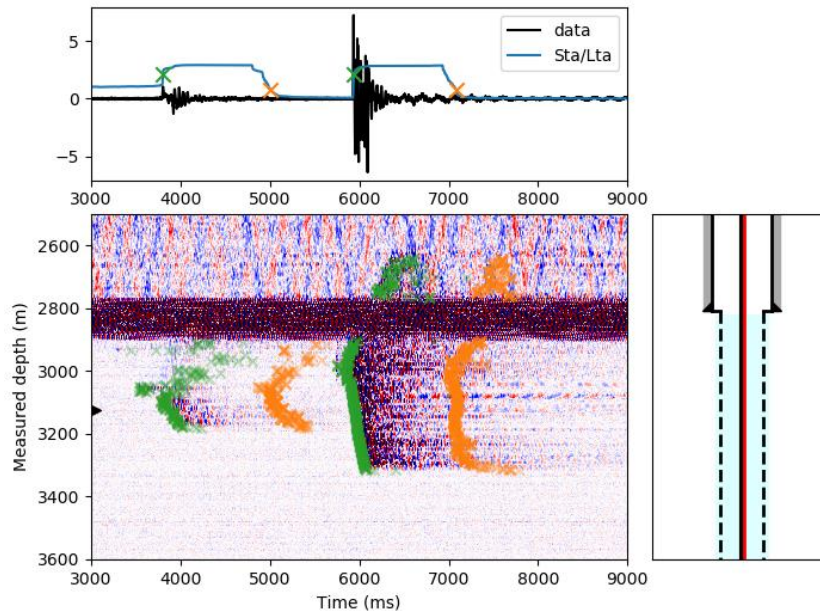
Figure 7: Spectrograms for a 250ms moving window at different depth along the well during the sudden vibrational event depicted in Figure 5. Red colors indicate high amplitudes, blue colors low amplitudes. The relative amplitudes are displayed by the same color ranges for all subplots.

378  
 379  
 380

381 **Event detection over time**

382

383 We applied a STA/LTA algorithm to automate the detection of the sudden vibrational events within the first 72  
384 minutes of cold-water fluid injection. Three attributes are obtained for each event: a) the depth location where the  
385 event starts b) the lower end and c) the upper end of the event according to the STA/LTA algorithm. Figure 8  
386 shows one example of the automated detection with the STA/LTA trigger. The upper subplot shows an example  
387 trace of raw DAS data at a depth of 3120 m MD (marked by the black arrow in the lower subplot) and the  
388 corresponding STA/LTA characteristic function. Beginning and end of the detection are marked by the green and  
389 orange crosses, respectively. The lower subplot shows spatio-temporal DAS data and the detection of two  
390 vibrational events.  
391

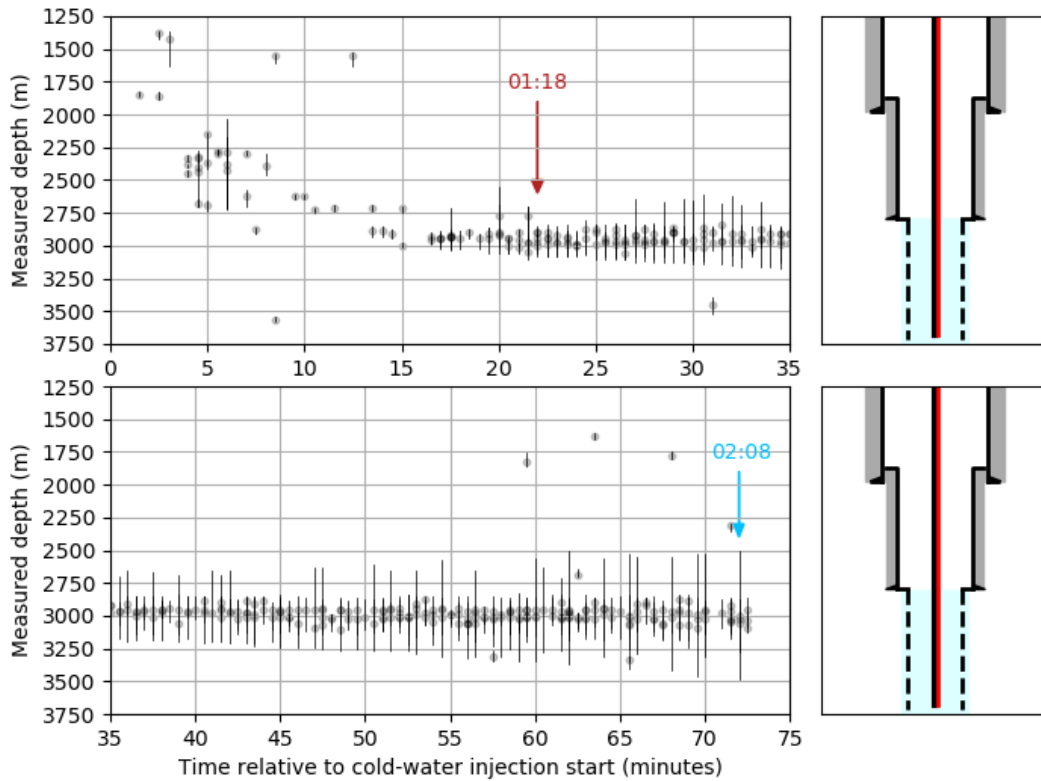


392

393 *Figure 8: STA/LTA trigger algorithm applied as an automated detection method for vibrational events. Trigger*  
394 *start and end is marked with green and orange crosses*

395 All vibrational events which occurred within the first 72 minutes of cold-water fluid injection are plotted in Figure  
396 9. Gray circles mark the spatio-temporal origin of vibrational events. The corresponding vertical black line  
397 indicates the spatial extent of the respective event. In this representation, events with a spatial extent of less than  
398 20 m are neglected. Such small events occur between 4-10 times per minute in the depth region from 1250-2750  
399 m MD over the entire investigated 72 minutes after fluid injection start. Within the first 15 minutes, only a  
400 relatively small number of bigger vibrational events occur, i.e. events which extend over more than 20m. Early  
401 events (within the first 5 minutes relative to injection start) appear in the depth region between 1250-1900 m MD.  
402 Except for two large events (4 minutes: 2260-2730 m MD and 6 minutes: 2040-2700 m MD), the spatial extent of  
403 the vibrational events is rather small. One single event was recorded at a depth of 3540-3580 m MD close to the  
404 shoe of the installation. With time, the depth of vibrational events increases to 2900 m MD. From 17 minutes  
405 onwards, the occurrence of vibrational events is mostly constrained in the depth region from 2900-3100 m MD.  
406 The maximum spatial extent of large vibrational events increases with time. From 01:18 (+22 minutes after  
407 injection start) onwards, most of the events extend into the depth region of 2835-3080 m MD. At 02:08 (+72  
408 minutes to injection start), the spatial extent of the events is 2500-3470 m MD.

409 With time, the frequency of the occurrence of the events decreases. 4-5 hours after injection start, large events  
410 (such as in Figure 6 C and D) appear every 10 – 15 minutes. 8 hours after injection start, large events appear  
411 approximately every 25 – 40 minutes.

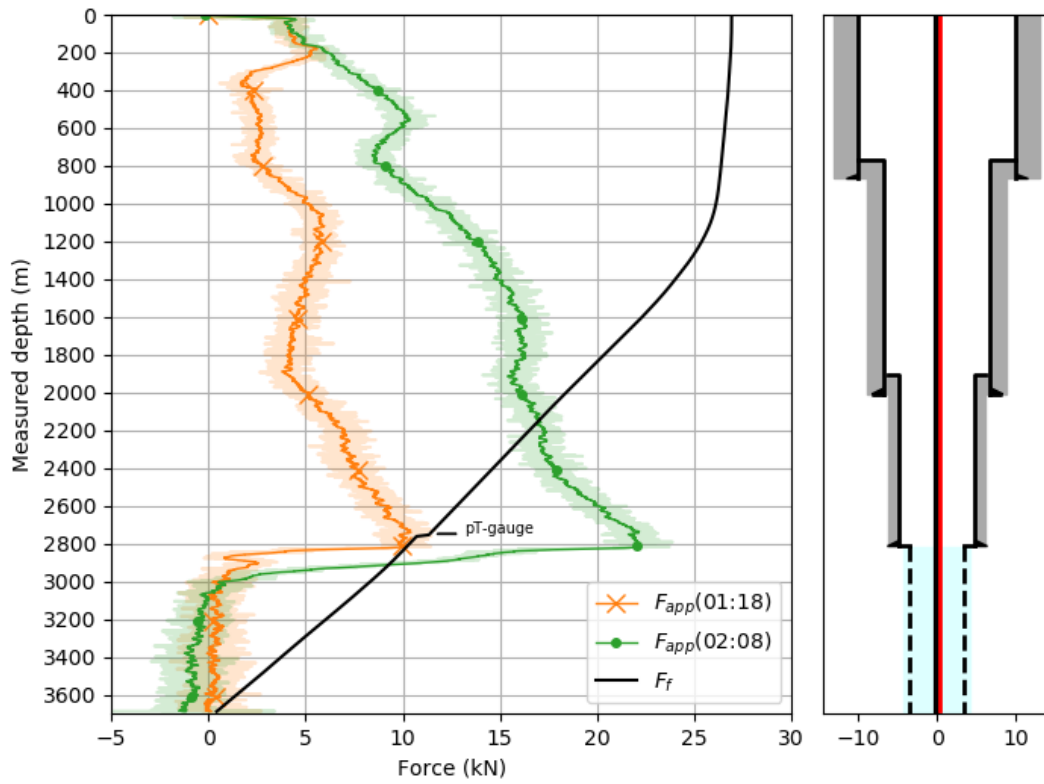


412  
 413 *Figure 9: Gray circles and black vertical lines indicate the spatio-temporal origin and spatial extent of vibrational*  
 414 *events in the well, respectively. The shown period comprises the first 72 minutes of cold-water fluid injection.*

415  
 416  
 417 **3.3 Friction force model**  
 418

419 The static friction force  $F_f$  after formula (3) is compared to the applied force from thermal contraction of the rod  
 420  $F_{app}$  after formula (5) which was evaluated for the period from injection start to 01:18 (+22 minutes after start of  
 421 injection) and to 02:08 (+72 minutes after start of injection) (Figure 10). The gravitational weight force  $F_w$  per  
 422 nylon centralizer is constant for every contact point of the rod. The force needed to overcome the cumulative static  
 423 friction  $F_f$  is a function of the borehole inclination.  $F_f$  increases from the bottom of the rod installation at 3691 m  
 424 MD towards 1000 m MD. The bottom end of the sucker rod and the carrier of the pT gauge at 2755 m MD create  
 425 an additional static friction force of 0.4 kN and 0.5 kN, respectively. Above 1000 m MD, the well is nearly vertical  
 426 and only little static friction is expected. The static friction  $F_f$  at 1000 m MD yields 26.1 kN.  $F_{app}$  at 01:18 is lower  
 427 than  $F_f$  for the entire installation length. Only in the depth interval 2731-2820 m MD,  $F_{app}$  approaches a force of  
 428 10.5 kN which is close to  $F_f$ . This indicates that forces are sufficient to initiate relative motion between sucker rod  
 429 and casing at that depth. With ongoing cold-water fluid injection, the applied forces  $F_{app}$  increase with further  
 430 decreasing temperatures. At 02:08,  $F_{app}$  surpasses the frictional forces in the depth range from 2150-2912 m MD.  
 431  $F_f$  and  $F_{app}$  intersect at 17.0 kN and 9.3 kN, respectively. At the depth interval from 2732-2820 m MD, the applied  
 432 force peaks at 22.0 kN (shown in Figure 10). For all estimates given above, it is assumed that the sucker rod did  
 433 not move relative to the casing, i.e., thermal stresses can build up but will not be released by relative motion.

434  
 435



436  
 437  
 438  
 439

Figure 10: Comparison of static friction  $F_f$  with applied forces  $F_{app}$  from thermal contraction of the rod within the first 72 minutes of cold-water fluid injection. The pale colors in  $F_{app}$  originate from measured DTS data and the solid lines are constructed by a moving average over 15 m

440  
 441

## 442 4. Discussion

443 With the help of distributed fiber-optic temperature and acoustic data, we monitored a cold-water injection period  
444 in a geothermal well at the site Schäftlarnstraße, Munich. The downhole monitoring data allows for an analysis of  
445 the deformation of the 3.6 km long sucker rod/fiber-optic cable construction due to cooling. We observe numerous  
446 localized episodes of large strain-rates that nucleate along the inclined stretch of the borehole and propagate both  
447 towards greater depth and the surface. Such events induce quickly declining elastic vibrations along the entire  
448 extent of the affected interval. The emergence of these vibrational events strongly correlates with the beginning of  
449 the fluid injection. In the following, we thus argue that the vibrational events are a result of the substantial  
450 temperature changes which the sucker rods with the optic fiber are exposed to. The contraction of the sucker rods  
451 upon cooling induces stress where the sucker rod is held to the borehole wall by frictional forces. On the basis of  
452 a simple mechanic model we show that accumulated stresses may eventually exceed the friction giving rise to  
453 sudden stress release and the observed strain changes.

### 454 4.1 Assessment of measuring errors

455 Our monitoring data analysis is based on a debatable approach of integrating DAS data over longer time periods.  
456 To obtain the  $\varepsilon_{DAS}$  profile over the period of 1 hour, a total number of 3.6 million strain rate profiles are integrated  
457 (sample rate: 1000 Hz). Such kind of numerical operation has a high risk of creating numerical errors due to e.g.  
458 rounding off or value truncation. In addition, the smallest systematic error in the DAS measurement system results  
459 in a significant drift over time which would misrepresent the strain profile measured by the sensing fiber. Also, it  
460 is well known that for FIMT type of installations, the gel filling allows for a creep and differential movement of  
461 fibers with respect to its surroundings which makes strain sensing unreliable for greater deformations and longer  
462 periods (e.g. [Lipus et al., 2018](#), [Becker et al., 2020](#)). However, a creep over many meters or even kilometers is  
463 most likely improbable. To strengthen the meaningfulness of our integrated strain profile, we analyzed the  $\varepsilon_{DAS}$  for  
464 a deeper section of the well, where little temperature change (ca. 1 °C) was measured by the DTS. In 3500 m  
465 depth, we do not observe any strain accumulation after temporal integration of strain rate data over a period of 60  
466 minutes. This indicates that the measured strain rate has no significant drift during the time of interest. For  
467 measurements with higher amplitudes such as within the depth interval 2800-2900 m, non-linear effects  
468 influencing the temporal integration of the data cannot be excluded.

### 469 4.2 DAS data integration

470 We integrated DAS data in time over 72 minutes to assess the absolute contraction of the rod construction prior to  
471 the cold-water injection start (see Figure 4). For the well interval from water table to the transition to the perforated  
472 liner, the results show a good match to the contraction that was theoretically assumed from the cooling of the well.  
473 However, from 2800-2900 m MD, we obtain much higher deformation from the DAS data than what we expected.  
474 We cannot give an unambiguous explanation for that but see two likely reasons for that observation. Firstly, the  
475 DAS integration process might result in a drift when integrating high amplitude DAS data. Especially from 2800-  
476 2900 m MD, constantly high energy is recorded by the system. The second explanation could be that the integrated  
477 DAS data measured a true deformation of the construction. In the depth region around 2800 m, the annular space  
478 of the borehole is rather irregular (transition to 7 “ liner interval, localized increase in the borehole inclination (see  
479 Figure 4, 3<sup>rd</sup> panel)). The repeating sudden sucker rod events might lead to an uneven distribution of the thermal  
480 stresses along the rod. Interestingly, the most prominent feed zone of the well coincides with the one single DAS  
481 interval which shows an extensional signal.  
482

483 The sudden slip events presented in this study show some similarity to the “slip events” which were previously  
484 observed in FIMT-type fiber-optic installation in a geothermal well ([Miller et al., 2018](#)). In the reported DAS  
485 campaign, a fiber-optic cable was installed in a geothermal well and it is argued that repeated thermal cycles led  
486 to a loss of frictional coupling between fiber-optic cable and the borehole wall. [Miller et al., 2018](#) reported that a  
487 sudden loss triggered a movement of the cable with a first arrival speed of 4600 m/s (we measured a first arrival  
488 speed of 4000 m/s). The integrated strain of the reported event shows a balance towards absolute contraction which  
489 we also observe in our events. Another similarity is given by the frequency content of these events. They recorded  
490 a dominant frequency of 45 Hz with some harmonics in both directions which we also observed in our data (see  
491 Figure 7 at 3000 m MD).

### 4.3 Stick-slip rod behaviour

We calculated the static friction force  $F_f$  along the rod construction by a cumulative sum of the friction of each nylon centralizer with the borehole inner wall. Independently of that, we computed the applied force  $F_{app}$  on the rod construction by thermal contraction using the DTS monitoring data. By comparing both curves, we can distinguish depth regions where the rod remains immobile ( $F_f > F_{app}$ ) and depth regions where the applied forces overcome the static friction force ( $F_f < F_{app}$ ). The temperature difference in the course of the investigated time period is particularly high over the 9 5/8" liner interval (depth region from 2485-2890 mMD) which in consequence also means that  $F_{app}$  is high. According to our model calculation, the contraction forces surpass the frictional forces at 2800 m MD around 01:18 (22 minutes after injection start). This result implies that after this time, the construction can contract in this depth interval. In other words, the thermal stresses on the rod construction in this depth region are high enough that the rod starts to move and to contract. Hence, the literature values assumed for the static friction between sucker rod and steel liner are assumed to approximate the real values.

With ongoing cold-water injection and further cooling of the well, the applied forces  $F_{app}$  increase. This leads to a continuous growing of the depth interval where  $F_{app}$  surpasses the static friction  $F_f$  of the rod. The STA/LTA detections match the predictions of the friction force model. After a rather quiet initial phase of low energetic events (before 17 minutes in Figure 9) which could be caused by the relaxation of previously accumulated stress anomalies along the sucker rods, repeated vibrational events start to concentrate in the region 2800-3100 m MD. As the region with  $F_f < F_{app}$  increases, the length of the vibrational events increases. From our friction force model, we would expect vibrational events (more specifically: the contraction part of the movement) at 02:08 in the depth region 2150-2910 m MD. However, the observed events extend from 2500-3500 m MD. Regarding the upper limit, we can see in Figure 10 that there is a significant change in slope for  $F_{app}$  at 02:08 at 2500 m MD. The friction force model is based on numerous assumptions (i.e. static friction coefficient nylon-steel, Young's modulus for stainless steel, neglecting fiber-optic cable, stress-free initial conditions) which might not accurately depict the downhole conditions. This could mean, that either the calculated applied force  $F_{app}$  is too high and/or the static friction force  $F_f$  is too low.

With respect to the lower limit of the vibrational events, we predict the contraction part ( $F_{app}(02:08)$  Figure 10) of the vibrational events down to a depth of 2912 m MD from our friction force model. However, we record vibrational events down to a depth of 3480 m MD. This discrepancy can partly be explained by the fact that the model prediction only shows the contraction part of the vibrational event. As seen in the cumulative strain  $\epsilon_{DAS}$  (see Figure 6 event A and B), the lowest part of a vibrational event yields extension. The most likely reason is that the contraction above results in a pulling of the rod from a lower lying region to compensate for the missing rod length. Therefore, the events can be traced down to a greater depth than predicted.

The constant temperature offset by +1 °C in the DTS profiles from 02:08 (relative to 01:18) in the depth interval from 3100 m MD to the end of the cable is unlikely to be caused by any fluid movement. While DTS temperature measurements did show a variation, no additional offset was recorded from the measured strain  $\epsilon_{DAS}$ . This could mean that the rod builds up thermal extensional stresses without actual movement taking place ( $\epsilon_{DTS} > 0$   $\epsilon_{DAS} = 0$ ). However, we speculate that the temperature anomaly is related to the processing of the DTS data. DTS temperature was measured in a double-ended configuration. A temperature profile is created by overlaying the DTS signal from both directions which are measured consecutively for both fiber branches. Close to the folding location (at the bottom of the well), an asymmetry in the temperature reading was observed between both fiber branches, which does not seem to be caused by any fluid motion. Averaging this difference between both branches led to a temperature offset. This offset was only visible if strong temperature changes were observed.

### 5. Conclusion

The field test at the geothermal site Schäftlarnstraße demonstrates that simultaneous recording of DTS and DAS data can be used for a detailed analysis of the deformation of a sucker rod type of fiber-optic cable installation in a 3.6 km deep well. By comparing the theoretical contraction of the rod structure from DTS with an estimated contraction from DAS, we can distinguish depth intervals with higher and lower thermal stresses in the material. We introduce a friction force model which accurately predicts the onset and extent of sucker rod events releasing accumulated thermal stress. This is an important finding for DAS monitoring in geothermal settings because it shows that localized high-energetic vibrational events must not necessarily be related to microseismic events



544 occurring in the rock formation but can originate in the subsurface construction and the way how the fiber-optic  
545 monitoring equipment is installed in the well. Moreover, the friction force model is useful to predict the data  
546 quality for DAS measurement campaigns for deep sucker-rod types of fiber-optic installations. Especially for the  
547 recordings of weak acoustic signals that are e.g. induced by fluid movement in the annulus, it is essential to know  
548 the potential sources of errors and artifacts in the data. During operations which introduce a temporal temperature  
549 gradient, thermo-mechanical response of freely hanging steel parts in the borehole may introduce stick-slip events  
550 that must be distinguished from any other relevant seismogenic source. Potentially, the vibrational energy from  
551 the sucker rod events can also be used to study the formation velocity in the near-field around the borehole.  
552 Furthermore, the large-scale contraction along certain sucker rod and fiber intervals must be considered with  
553 respect to the location of the distributed sensor nodes. Our description also serves as a starting point for a more  
554 detailed dynamic description of the observed processes. This can be of use to predict onset and depth interval of  
555 such sucker rod events and to contain their destructive potential in case of too quick cooling of the construction.

#### 556 **Code and data availability**

557 Python scripts and data are available upon request to the corresponding author.

#### 558 **Author contributions**

559 TR and KZo conceptualized, planned and coordinated the monitoring campaign. MPL, FS, CW, TR and DP  
560 conducted the field measurement. MPL performed the DAS data processing. All authors contributed in the  
561 interpretation of the results. MPL prepared the first draft of the manuscript with the contribution from all authors.

#### 562 **Competing interests**

563 The authors declare that they have no conflict of interest.

#### 564 **Special issue statement**

565 This article is part of the special issue “Fibre-optic sensing in Earth sciences”. It is not associated with a conference.

#### 566 **Financial support**

567 The fiber-optic cable was installed in the framework of the Geothermal Alliance Bavaria project, funded by the  
568 Bavarian Ministry of Economic Affairs, Energy and Technology. A part of this work was financed by the  
569 GeConnect project (Geothermal Casing Connections for Axial Stress Mitigation), coordinated by ÍSOR, which is  
570 funded through the ERANET cofund GEOTHERMICA (Project no. 731117), from the European Commission,  
571 Technology Development Fund (Iceland), Bundesministerium für Wirtschaft und Energie aufgrund eines  
572 Beschlusses des Deutschen Bundestages (Germany) and Ministerie van Economische Zaken (The Netherlands).

#### 573 **Acknowledgements**

574 This work would not have been possible without the continuous support from our partners involved in the project.  
575 The authors are thankful to Stadtwerke München, owner and operator of the geothermal site Schäftlarnstraße, for  
576 providing access to the well site, their premises and well data. The authors would also like to thank the drilling  
577 contractor Daldrup for accessing the site during the drilling and well completion operation. Moreover, we would  
578 like to give credit to our colleagues at Erdwerk GmbH and Baker Hughes for the close collaboration and fruitful  
579 discussions. From GFZ, the authors are thankful to Christian Cunow and Tobias Raab who supported the field  
580 work and acquisition of fiber-optic data. The authors would like to thank Mr. Ryan Schultz and the second  
581 anonymous referee for reviewing and improving this manuscript.

582

583 **References**

- 584
- 585 Allen, R. V. "Automatic earthquake recognition and timing from single traces." *Bulletin of the Seismological*
- 586 *Society of America*, 1978.
- 587 Becker, M. W., C. Ciervo, M. Cole, T. Coleman, and M. Mondanos. "Fracture hydromechanical response
- 588 measured by fiber optic distributed acoustic sensing at milliHertz frequencies." *Geophys. Res. Lett.* *44*,
- 589 2017, doi:10.1002/2017GL073931.
- 590 Becker, M. W., T. I. Coleman, and C. C. Ciervo. "Distributed Acoustic Sensing as a Distributed Hydraulic
- 591 Sensor in Fractured Bedrock." *Water Resources Research*, *56*, 2020, doi:10.1029/2020WR028140.
- 592 Berman, A. D., W. A. Ducker, and J. N. Israelachvili. "Origin and Characterization of Different Stick-Slip
- 593 Friction Mechanisms." *Langmuir*, 1996, doi:10.1021/la950896z.
- 594 Bruno, M. S. "Use of Fiber Optic Distributed Acoustic Sensing for Measuring Hydraulic Connectivity for
- 595 Geothermal Applications." Tech. rep., GeoMechanics Technologies, U.S. Department of Energy/Small
- 596 Business Innovation Research, Bruno2018.
- 597 Bücken, C., and S. Grosswig. "Distributed temperature sensing in the oil and gas industry - insights and
- 598 perspectives." *Oil Gas European Magazine* *43* (2017).
- 599 Cardarelli, F. "Ferrous Metals and Their Alloys." In: *Materials Handbook*. Springer, Cham., 2018,
- 600 doi:10.1007/978-3-319-38925-7\_2.
- 601 Chang, H., and N. Nakata. "Investigation of the time-lapse changes with the DAS borehole data at the Brady
- 602 geothermal field using deconvolution interferometry." *SEG Technical Program Expanded Abstracts* :  

603 *3417-3421*, 2020, doi:10.1190/segam2020-3426023.1.

604 Daley, T. M., D. E. Miller, K. Dodds, P. Cook, and B. M. Freifeld. "Field testing of modular borehole

605 monitoring with simultaneous distributed acoustic sensing and geophone vertical seismic profiles at

606 Citronelle, Alabama." *Geophysical Prospecting*, 2016, doi:10.1111/1365-2478.12324

607 Daley, T. M., et al. "Field testing of fiber-optic distributed acoustic sensing (DAS) for subsurface seismic

608 monitoring." *The Leading Edge*, 2013, doi:10.1190/tle32060699.1

609 Finfer, D. C., V. Mahue, S. Shatalin, T. Parker, and M. Farhadiroushan. "Borehole Flow Monitoring using a

610 Non-intrusive Passive Distributed Acoustic Sensing (DAS)." *Society of Petroleum Engineers*, 2014,

611 doi:10.2118/170844-MS

612 Förster, A., J. Schrötter, D. F. Merriam, and D. D. Blackwell. "Application of optical-fiber temperature logging -

613 an example in a sedimentary environment." *Geophysics* *62*(4) (1997), doi:10.1190/1.1444211

614 Ghahfarokhi, P. K., T. Carr, L. Song, P. Shukla, and P. Pankaj. "Seismic Attributes Application for the

615 Distributed Acoustic Sensing Data for the Marcellus Shale: New Insights to Cross-Stage Flow

616 Communication." *Society of Petroleum Engineers*, 2018, doi:10.2118/189888-MS

617 Götz, J., S. Lüth, J. Hennings, and T. Reinsch. "Vertical seismic profiling using a daisy-chained deployment of

618 fibre-optic cables in four wells simultaneously – Case study at the Ketzin carbon dioxide storage site." *Geophysical Prospecting*, 2018, doi:10.1111/1365-2478.12638

619 Harris, K., D. White, D. Melanson, C. Samson, and T. M. Daley. "Feasibility of time-lapse VSP monitoring at

620 the Aquistore CO2 storage site using a distributed acoustic sensing system." *International Journal of*

621 *Greenhouse Gas Control*, 2016, doi:10.1016/j.ijggc.2016.04.016

622 Hartog, A. H. "A Distributed Temperature Sensor Based on Liquid-Core Optical Fibers." *Journal of Lightwave*

623 *Technology*, 1983, doi:10.1109/JLT.1983.1072146

624 Hartog, A. H., and G. Gamble. "Photonic distributed sensing." *Physics World*, 1991, doi:10.1088/2058-

625 7058/4/3/30

626 Hennings, J., E. Huenges, and H. Burkhardt. "In situ thermal conductivity of gas-hydrate-bearing sediments of

627 the Mallik 5L-38 well." *Journal of Geophysical Research* *110* (2005), doi:10.1029/2005JB003734

628 Hennings, J., E. Martuganova, M. Stiller, B. Norden, and C. M. Krawczyk. "Wireline distributed acoustic

629 sensing allows 4.2 km deep vertical seismic profiling of the Rotliegend 150 °C geothermal reservoir in

630 the North German Basin." *Solid Earth* *12*, 2021, doi:10.5194/se-12-521-2021

631 Hidnert, P. "Thermal Expansion of Heat Resisting Alloys (nickel-chromium, Iron-chromium and Nickel

632 Chromium-iron Alloys)." *Bureau of Standards Journal of Research*, 1931.

633 Hurtig, E., S. Grosswig, M. Jobmann, K. Kühn, and P. Marschall. "Fibre-optic temperature measurements in

634 shallow boreholes: experimental application for fluid logging." *Geothermics* *23* (1994),

635 doi:10.1016/0375-6505(94)90030-2

636

637 Johannessen, K., B. K. Drakeley, and M. Farhadiroushan. "Distributed Acoustic Sensing - A New Way of  
638 Listening to Your Well/Reservoir." *Society of Petroleum Engineers*, 2012, doi:10.2118/149602-MS

639 Lee, C. H., and A. A. Polycarpou. "Static Friction Experiments and Verification of an Improved Elastic-Plastic  
640 Model Including Roughness Effects." *Journal of Tribology*, 2007, doi:10.1115/1.2768074

641 Lipus, M. P., T. Reinsch, T. B. Weisenberger, S. Kragset, A. Stefánson, and S. G. Bogason. "Monitoring of a  
642 reverse cement job in a high temperature geothermal environment." *Geothermal Energy*, 2021,  
643 doi:10.1186/s40517-021-00187-y

644 Lipus, M., T. Reinsch, C. Schmidt-Hattenberger, J. Henninges, and M. Reich. "Gravel Pack Monitoring With a  
645 Strain Sensing Fiber Optic Cable." *Oil Gas European Magazine 4*, 2018, doi:10.19225/181202

646 Martuganova, E., M. Stiller, K. Bauer, J. Henninges, and C. M. Krawczyk. "Cable reverberations during wireline  
647 distributed acoustic sensing measurements: their nature and methods for elimination." *Geophys.*  
648 *Prospect.*, 2021, doi:10.1111/1365-2478.13090

649 Masoudi, A., M. Balal, and T. P. Newson. "A distributed optical fibre dynamic strain sensor based on phase-  
650 OTDR." *Meas. Sci. Technol.* 24, 2013, doi:10.1088/0957-0233/24/8/085204

651 Mateeva, A., et al. "Distributed acoustic sensing for reservoir monitoring with vertical seismic profiling."  
652 *Geophysical Prospecting*, 2014, doi:10.1111/1365-2478.12116

653 Miller, D. E., et al. "DAS and DTS at Brady Hot Springs: Observations about Coupling and Coupled  
654 Interpretations." *PROCEEDINGS, 43rd Workshop on Geothermal Reservoir Engineering Stanford*  
655 *University, Stanford, California, February 12-14, 2018.* 2020.

656 Munn, J. D., T. J. Coleman, B. I. Parker, M. J. Mondanos, and A. Chalari. "Novel cable coupling technique for  
657 improved shallow distributed acoustic sensor VSPs." *Journal of Applied Geophysics*, 2017,  
658 doi:10.1016/j.jappgeo.2017.01.007

659 Muraki, M., E. Kinbara, and T. Konishi. "A laboratory simulation for stick-slip phenomena on the hydraulic  
660 cylinder of a construction machine." *Tribology International*, 2003, doi:10.1016/S0301-  
661 679X(03)00054-9

662 Naldrett, G., C. Cerrahoglu, and V. Mahue. "Production Monitoring Using Next-Generation Distributed Sensing  
663 Systems." *Society of Petrophysicists and Well-Log Analysts*, 2018.

664 Pearce, J. G., et al. "High Resolution, Real-Time Casing Strain Imaging for Reservoir and Well Integrity  
665 Monitoring: Demonstration of Monitoring Capability in a Field Installation." *SPE Annual Technical*  
666 *Conference and Exhibition*, 2009.

667 Raab, T., T. Reinsch, S. R. Aldaz Cifuentes, and J. Henninges. "Real-Time Well-Integrity Monitoring Using  
668 Fiber-Optic Distributed Acoustic Sensing." *Society of Petroleum Engineers*, 2019, doi:10.2118/195678-  
669 PA

670 Reinsch, T., J. Henninges, and R. Ásmundsson. "Thermal, mechanical and chemical influences on the  
671 performance of optical fibres for distributed temperature sensing in a hot geothermal well."  
672 *Environmental Earth Science* 70 (2013), doi:10.1007/s12665-013-2248-8

673 Reinsch, T., T. Thurley, and P. Jousset. "On the mechanical coupling of a fiber optic cable used for distributed  
674 acoustic/vibration sensing applications—a theoretical consideration." *Measurement Science and*  
675 *Technology*, 2017, doi:10.1088/1361-6501/aa8ba4

676 Schölderle, F., et al. "Monitoring Cold Water Injections for Reservoir Characterization using a Permanent Fibre  
677 Optic Installation in a Geothermal Production Well in the Southern German Molasse Basin."  
678 *Geothermal Energy (in review)*, 2021, doi:10.1186/s40517-021-00204-0

679 Storch, T., T. Grab, U. Gross, and S. Wagner. "VISUAL OBSERVATIONS INSIDE A GEOTHERMAL  
680 THERMOSYPHON." *Heat Pipe Science and Technology, An International Journal* 4 (2013): 217–226,  
681 doi:10.1615/HeatPipeScieTech.2014011210

682 Sun, Y., Z. Xue, H. Park, T. Hashimoto, and Y. Zhang. "Optical Sensing of CO2 Geological Storage Using  
683 Distributed Fiber-Optic Sensor: From Laboratory to Field-Scale Demonstrations." *Energy Fuels*, 2020,  
684 doi:10.1021/acs.energyfuels.0c03925

685 ToolBox, The Engineering. "Elastic Properties and Young Modulus for some Materials." *The Engineering*  
686 *ToolBox. Retrieved January 6, 2012.*, 2012.

687 Vaezi, Y., and M. van der Baan. "Comparison of the STA/LTA and power spectral density methods for  
688 microseismic event detection." *Geophysical Journal International*, 2015, doi:10.1093/gji/ggv419

689 Zhang, Y., X. Lei, T. Hashimoto, and Z. Xue. "Towards retrieving distributed aquifer hydraulic parameters from  
690 distributed strain sensing." *Journal of Geophysical Research Solid Earth*, 2020,  
691 doi:10.1029/2020JB020056  
692